

University of Groningen

Systematic errors in strong gravitational lensing reconstructions, a numerical simulation perspective

Enzi, Wolfgang; Vegetti, Simona; Despali, Giulia; Hsueh, Jen-Wei; Metcalf, R. Benton

Published in:
Monthly Notices of the Royal Astronomical Society

DOI:
[10.1093/mnras/staa1224](https://doi.org/10.1093/mnras/staa1224)

IMPORTANT NOTE: You are advised to consult the publisher's version (publisher's PDF) if you wish to cite from it. Please check the document version below.

Document Version
Publisher's PDF, also known as Version of record

Publication date:
2020

[Link to publication in University of Groningen/UMCG research database](#)

Citation for published version (APA):

Enzi, W., Vegetti, S., Despali, G., Hsueh, J-W., & Metcalf, R. B. (2020). Systematic errors in strong gravitational lensing reconstructions, a numerical simulation perspective. *Monthly Notices of the Royal Astronomical Society*, 496(2), 1718-1729. <https://doi.org/10.1093/mnras/staa1224>

Copyright

Other than for strictly personal use, it is not permitted to download or to forward/distribute the text or part of it without the consent of the author(s) and/or copyright holder(s), unless the work is under an open content license (like Creative Commons).

The publication may also be distributed here under the terms of Article 25fa of the Dutch Copyright Act, indicated by the "Taverne" license. More information can be found on the University of Groningen website: <https://www.rug.nl/library/open-access/self-archiving-pure/taverne-amendment>.

Take-down policy

If you believe that this document breaches copyright please contact us providing details, and we will remove access to the work immediately and investigate your claim.

Downloaded from the University of Groningen/UMCG research database (Pure): <http://www.rug.nl/research/portal>. For technical reasons the number of authors shown on this cover page is limited to 10 maximum.

Systematic errors in strong gravitational lensing reconstructions, a numerical simulation perspective

Wolfgang Enzi,¹★ Simona Vegetti,¹ Giulia Despali^①,¹ Jen-Wei Hsueh²
and R. Benton Metcalf^{3,4}

¹Max Planck Institute for Astrophysics, Karl-Schwarzschild-Strasse 1, Garching bei München, DE-85748, Germany

²Kapteyn Astronomical Institute, University of Groningen, P.O. Box 800, NL-9700AV, Groningen, the Netherlands

³Dipartimento di Fisica & Astronomia, Università di Bologna, via Gobetti 93/2, I-40129 Bologna, Italy

⁴INAF-Osservatorio Astronomico di Bologna, via Ranzani 1, I-40127 Bologna, Italy

Accepted 2020 April 26. Received 2020 April 9; in original form 2019 November 6

ABSTRACT

We present the analysis of a sample of 24 SLACS-like galaxy–galaxy strong gravitational lens systems with a background source and deflectors from the Illustris-1 simulation. We study the degeneracy between the complex mass distribution of the lenses, substructures, the surface brightness distribution of the sources, and the time delays. Using a novel inference framework based on Approximate Bayesian Computation, we find that for all the considered lens systems, an elliptical and cored power-law mass density distribution provides a good fit to the data. However, the presence of cores in the simulated lenses affects most reconstructions in the form of a Source Position Transformation. The latter leads to a systematic underestimation of the source sizes by 50 per cent on average, and a fractional error in H_0 of around 25^{+37}_{-19} per cent. The analysis of a control sample of 24 lens systems, for which we have perfect knowledge about the shape of the lensing potential, leads to a fractional error on H_0 of 12^{+6}_{-3} per cent. We find no degeneracy between complexity in the lensing potential and the inferred amount of substructures. We recover an average total projected mass fraction in substructures of $f_{\text{sub}} < 1.7\text{--}2.0 \times 10^{-3}$ at the 68 per cent confidence level in agreement with zero and the fact that all substructures had been removed from the simulation. Our work highlights the need for higher resolution simulations to quantify the lensing effect of more realistic galactic potentials better, and that additional observational constraint may be required to break existing degeneracies.

Key words: gravitational lensing: strong – galaxies: haloes – galaxies: structure.

1 INTRODUCTION

Galaxy–galaxy strong gravitational lensing is a powerful tool to investigate a large number of diverse astrophysical and cosmological inquiries (see Treu 2010, and references therein). For example, in the detailed analysis of the physical and kinematical properties of distant galaxies strong lensing provides the magnification that allows one to overcome the observational limitations of low signal-to-noise ratio and spatial resolution (e.g. Shirazi et al. 2014; Rybak et al. 2015; Rizzo et al. 2018; Spingola et al. 2019). Measurements of the time delay between the multiple lensed images of time-varying sources have been demonstrated to provide a promising constraint on the Hubble constant H_0 and weak constraints on other cosmological parameters (e.g. Suyu et al. 2010; Chen et al. 2019;

Wong et al. 2019). The sensitivity of lensing to total mass has been used to quantify the amount of low-mass dark matter haloes and thereby the properties of dark matter, both with lensed quasars (Mao & Schneider 1998; Nierenberg et al. 2014; Gilman et al. 2019; Hsueh et al. 2019) and lensed galaxies (Koopmans 2005; Vegetti & Koopmans 2009b; Vegetti et al. 2010; Vegetti et al. 2012; Hezaveh et al. 2016).

In order for these studies to be robust, a good understanding of the lenses gravitational potential is essential. For example, Ritondale et al. (2019) have shown from the analysis of the BELLS GALLERY samples, that in certain cases it is necessary to extend the lensing mass density distribution beyond the standard assumption of a single or multiple power laws in order to obtain a correct focusing of the reconstructed background source. Using hydrodynamical simulations, Xu et al. (2017) have shown that power-law mass models can bias the inference on the Hubble constant by up to 50 per cent, a deviation that is related to the mass sheet degeneracy

★ E-mail: enzi@mpa-garching.mpg.de

(MSD; Falco, Gorenstein & Shapiro 1985). Using both numerical simulations and mock observations, Gilman et al. (2018) and Hsueh et al. (2018) have demonstrated that complex baryonic structures in elliptical galaxies can contribute to 8–10 per cent of the strength of flux-ratio anomalies, and therefore constitute a potential bias in the inferred properties of dark matter (see also Möller, Hewett & Blain 2003; Xu et al. 2015). Similarly, Hsueh et al. (2016, 2017) have shown that lens galaxies with a significant edge-on disc are characterized by strong flux-ratio anomalies that can be explained by the presence of the disc without the need to include a significant population of substructures. Recently, from the analysis of extended lensed images from the BELLS GALLERY sample, Ritondale et al. (2019) have concluded that complex mass distributions can emulate the effects of substructures and, therefore, lead to false-positive detections. More generally, Unruh, Schneider & Sluse (2017) have shown that source position transformations (Schneider & Sluse 2014) can explain why independent studies of the same lens system may result in different inferred lens parameters.

In this work, we quantify the systematic errors that may be induced by departures from simple power-law lensing mass distribution on the different lensing observables using galaxies taken from the cosmological hydrodynamical simulation Illustris-1 (Vogelsberger et al. 2014). We remove all substructures from the simulations and create mock lensing observations emulating the SLACS (Bolton et al. 2006) survey. We then model these data using a novel inference approach based on Approximate Bayesian Computation (ABC), under the classical assumption of a cored power-law mass model. We then infer the fraction of projected mass contained in substructures f^{sub} to quantify the degeneracy between substructures, time delays (which are relevant in the determination of H_0), other forms of complexity in the lensing potential, and the source surface brightness distribution. The paper is structured as follows: in Section 2, we give a short overview of the Illustris-1 simulations and specify how we create mock data. In Section 3, we describe the physical model as well as the statistical method that we use for the reconstruction of the mock data. In Section 4, we present and discuss our results. In Section 5, we conclude our study by summarizing our main findings.

2 LENSING DATA GENERATION

In order to study the lensing signal from galaxies with complex mass distributions, we focus on simulated galaxies from the hydrodynamical numerical simulation Illustris-1. In this section, we provide a short description of the simulation and how we generated mock lensing observations from it.

2.1 Lens and source galaxies selection

The Illustris-1 project is a series of hydrodynamical numerical simulations of cosmological volumes that follow the evolution of dark matter, cosmic gas, stars, and supermassive black holes from a starting redshift of $z = 127$ to the present time, all while accounting for realistic baryonic physics. In this work, we use the main run of Illustris-1, which has a box size of 106.5 Mpc in all three dimensions and contains 1820^3 dark matter particles and (initial) gas cells. The simulations were run using the moving-mesh AREPO code (Springel 2010; Nelson 2015). The dark matter particle mass is $6.3 \times 10^6 M_\odot$ and the initial gas particle mass is $1.3 \times 10^6 M_\odot$, while the simulation uses softening lengths for dark matter and baryons that are $\epsilon_{\text{dm}} = 1.4$ kpc and $\epsilon_b = 0.7$ kpc, respectively. The simulations adopt the cosmological parameters $\Omega_m = 0.2726$, $\Omega_\Lambda = 0.7274$, $\Omega_b =$

0.0456 , $\sigma_8 = 0.809$, $n_s = 0.963$, and $H_0 = 100 h \times \text{km s}^{-1}/\text{Mpc}$ with $h = 0.704$, which are consistent with the latest Wilkinson Microwave Anisotropy Probe 9 measurements (Hinshaw et al. 2013).

From the catalogue of Illustris-1, we choose 10 galaxies at redshift $z = 0.2$ to be our sample of lenses. These are analogues of the SLACS lenses (Bolton et al. 2006) and were selected by Despali & Vegetti (2017) based on a number of properties: the total halo mass, stellar mass of the central galaxy, stellar effective radius, velocity dispersion, and dynamical properties compatible with an early-type morphology. In particular, they selected galaxies according to the fraction of stellar mass showing specific circularities $\epsilon = J_z/J(E)$, where J_z is the angular momentum of an individual stellar particle and $J(E)$ is the maximum angular momentum within its local environment. The fractions $f_\epsilon < 0.0$ and $f_\epsilon > 0.7$ are indicators of an early-type morphology (see e.g. Genel et al. 2015; Teklu et al. 2015), typical for lens galaxies at the considered redshift.

This selection ensures that we avoid galaxies with a significant disc component, for which the lensing properties have already been investigated by Hsueh et al. (2018). In Table 1, we list the main properties of the considered sample of lens galaxies. We also select a compact Illustris-1 galaxy at redshift $z = 0.6$ as our background source to be lensed. We use the same source galaxy for all created mocks.

2.2 Ray tracing

For each of the 10 lens galaxies in our sample, we consider the projection of their mass density distribution on to the three principal planes and use the ray-tracing code GLAMER (Metcalf & Petkova 2014; Petkova, Metcalf & Giocoli 2014)¹ to generate 3×10 maps of the lensed source surface brightness distribution. The focus of this paper is on the lensing effect of small-scale complexity in the lens mass distribution such as dense baryonic structures from tidally disrupted satellites and general departures from simple single power-law models. Therefore, we have removed all particles belonging to dark matter substructures and only considered the contribution from the main halo. However, it is worth mentioning that in the Illustris-1 simulation, the minimum resolved substructure mass is of the order of $\simeq 10^8 M_\odot$. For each main halo, we take all its particles within $R_{200} \approx R_{\text{vir}}$ as identified by the SUBFIND algorithm (Springel et al. 2001).

For a given collection of particles (i.e. their positions, masses, and smoothing lengths as used in the original simulation), GLAMER determines the corresponding deflection angle maps with an efficient tree algorithm. In order to avoid unrealistic deflections of the light rays, each particle is represented by a B-spline in three dimensions, as it is commonly done in smooth particle hydrodynamic (SPH) simulations. We set the size of the smoothing length to the distance of the N^{smooth} -th nearest neighbour. We choose $N^{\text{smooth}} = 64$, which corresponds to scales $\lesssim \mathcal{O}(\text{kpc})$. This scheme provides smaller smoothing lengths where the particles are dense (e.g. at the centres of haloes), and larger ones where the particles are sparse and shot noise would otherwise pose a problem. We follow a similar approach for the baryonic cells by treating them as particles with a corresponding smoothing length in order to make them compatible with the implementation of GLAMER. The minimum and average smoothing lengths over the whole sample

¹<http://glenco.github.io/glamer/>

Table 1. The properties of the lens galaxies selected from the Illustris-1 simulation. From left to right, we list the virial mass M_{vir} , the mass of the dark matter component M_{dm} , the stellar mass M_* , the gas mass M_{gas} , the fraction of stellar mass showing a circularity higher than 0.7 $f_{\epsilon > 0.7}$ and lower than 0.0 $f_{\epsilon < 0.0}$, as well as the virial radius r_{vir} and stellar radius r_* .

ID_{fof}	M_{vir} $M_{\odot} h^{-1}$	M_{dm} $M_{\odot} h^{-1}$	M_* $M_{\odot} h^{-1}$	M_{gas} $M_{\odot} h^{-1}$	$f_{\epsilon > 0.7}$ 1	$f_{\epsilon < 0.0}$ 1	r_{vir} $\text{kpc } h^{-1}$	r_* $\text{kpc } h^{-1}$
28	2.314e+13	1.910e+13	4.107e+11	1.582e+11	1.580e−01	6.522e−01	6.319e+02	1.025e+01
40	2.789e+13	2.404e+13	5.945e+11	1.396e+11	1.662e−01	6.563e−01	6.725e+02	1.458e+01
51	2.094e+13	1.906e+13	4.691e+11	8.335e+10	7.534e−02	9.388e−01	6.112e+02	1.205e+01
55	2.327e+13	1.953e+13	4.341e+11	2.664e+11	1.323e−01	7.430e−01	6.330e+02	1.539e+01
65	1.749e+13	1.543e+13	6.486e+11	3.023e+10	1.284e−01	8.440e−01	5.756e+02	1.916e+01
84	1.179e+13	1.134e+13	3.427e+11	5.861e+10	1.664e−01	7.242e−01	5.047e+02	1.411e+01
91	1.355e+13	1.085e+13	2.147e+11	2.446e+10	6.730e−02	8.781e−01	5.286e+02	8.816e+00
95	1.094e+13	9.443e+12	3.164e+11	1.371e+11	5.936e−02	9.282e−01	4.922e+02	1.225e+01
121	6.297e+12	5.658e+12	1.389e+11	1.550e+11	1.085e−01	7.531e−01	4.095e+02	2.656e+00
140	8.737e+12	7.818e+12	2.268e+11	4.465e+10	1.077e−01	7.056e−01	4.567e+02	7.336e+00

are 0.6–0.8 kpc and 16 kpc, respectively, which also taking into account the softening length of the simulation tell us that we can safely resolve inhomogeneities on scales $> \mathcal{O}(\text{kpc})$. Notice that the pixel size of the mock images is 0.04 arcsec.

As an example, Fig. 1 shows the convergence maps (i.e. surface mass density normalized by the critical surface mass density) of three representative Illustris-1 galaxies. The presence of small-scale features in the mass distribution, which are typically not captured by simplified parametric profiles, are highlighted by the irregular iso-convergence contours.

The galaxies in the Illustris-1 sample show unrealistically large cores. This effect is a well-known challenge for simulations and arises from finite smoothing lengths. Depending on the lensing configuration, these large cores lead to lensed images with morphologies (see the middle-bottom panel of Fig. 1 for an example) that are rarely observed in real gravitational lens systems, where the central mass density distribution may be cuspiers. For this reason, we remove six realizations from our set and in the following we will only focus on the 24 systems with realistic lensed images. A similar problem was recently identified by Mukherjee et al. (2018) in a study of the EAGLE simulation (Schaye et al. 2015).

2.3 Observational effects

In order to generate mock *HST* observations, we convolve the lensed surface brightness distribution $I(\mathbf{x})$ with the point spread function (PSF) $p(\mathbf{x})$ from the WFC3 camera in the F606W filter and add the contribution of observational noise. In particular, for each of the lensed images in our sample, we draw a realization of Gaussian random noise $\mathbf{n}(\mathbf{x})$, with

$$P(\mathbf{n}|\mathbf{N}) = \mathcal{G}(\mathbf{n}, \mathbf{N}) := \exp\left(-\frac{1}{2}\mathbf{n}^T \mathbf{N}^{-1} \mathbf{n}\right) / \sqrt{\det(2\pi\mathbf{N})}, \quad (1)$$

which includes the contribution of a constant background b and another term proportional to the signal, which approximates the Poisson noise of photon counts. We assume the noise to be uncorrelated and therefore entries of the covariance matrix are multiplied by the Kronecker delta δ_{ij}^K :

$$\mathbf{N}_{ij} = [b + (p * I)(\mathbf{x}_i)] \times \delta_{ij}^K. \quad (2)$$

The level of noise is chosen in such a way to match the signal-to-noise ratio of the SLACS lenses analysed by Vegetti et al. (2014).

3 LENS MODELLING

In this section, we discuss the physical components that define our inference problem and present a novel inference approach based on ABC. For an overview on ABC in cosmology, we refer the reader to Akeret et al. (2015) and to Birrer, Amara & Refregier (2017) and Gilman et al. (2018, 2019) for examples of applications in the context of strong gravitational lensing.

3.1 Physical model

The physical model includes the following unknown components: the surface brightness distribution of the source galaxy, the mass distribution of the lens galaxy, and the amount of lens-galaxy mass contained in substructures.

3.1.1 Source surface brightness distribution

We follow Vegetti & Koopmans (2009a) and define the source surface brightness distribution $s(\mathbf{x})$ on an adaptive grid, so that $s_i = s(\mathbf{x}_i)$ corresponds to the brightness value at the position \mathbf{x}_i of the i th vertex of a Delaunay mesh. The mesh vertices are obtained by ray tracing a subset of the pixels of the observed data $d(\mathbf{x})$ to the source plane. The source surface brightness at each vertex constitutes a free nuisance parameter of the model, while the source brightness within the triangles spanned by these vertices is determined via linear interpolation.

3.1.2 Lens projected mass distribution

We parametrize the projected mass distribution of the main deflector with an elliptical cored power-law profile of convergence

$$\kappa(\rho) = \frac{\kappa_0 \left(2 - \frac{\gamma}{2}\right) q^{-1/2}}{2 \left(r_c^2 + \rho^2\right)^{(\gamma-1)/2}}, \quad (3)$$

where κ_0 is the amplitude, γ is the 3D slope, q is the projected minor-to-major axial ratio in projection, θ is the angular orientation of the major axis (defined north to east), x_0 and y_0 are the centre position coordinates, and r_c is the core radius. After a rotation by θ and a translation of (x_0, y_0) , the ellipse radius ρ is defined via $\rho^2 = x^2 + y^2/q^2$. Together with the strength Γ and position angle Γ_θ of an external shear component, these geometrical parameters constitute part of the key target parameters in the reconstruction process and we collectively refer to them as macro-model parameters or $\eta^{\text{macro}} = (\kappa_0,$

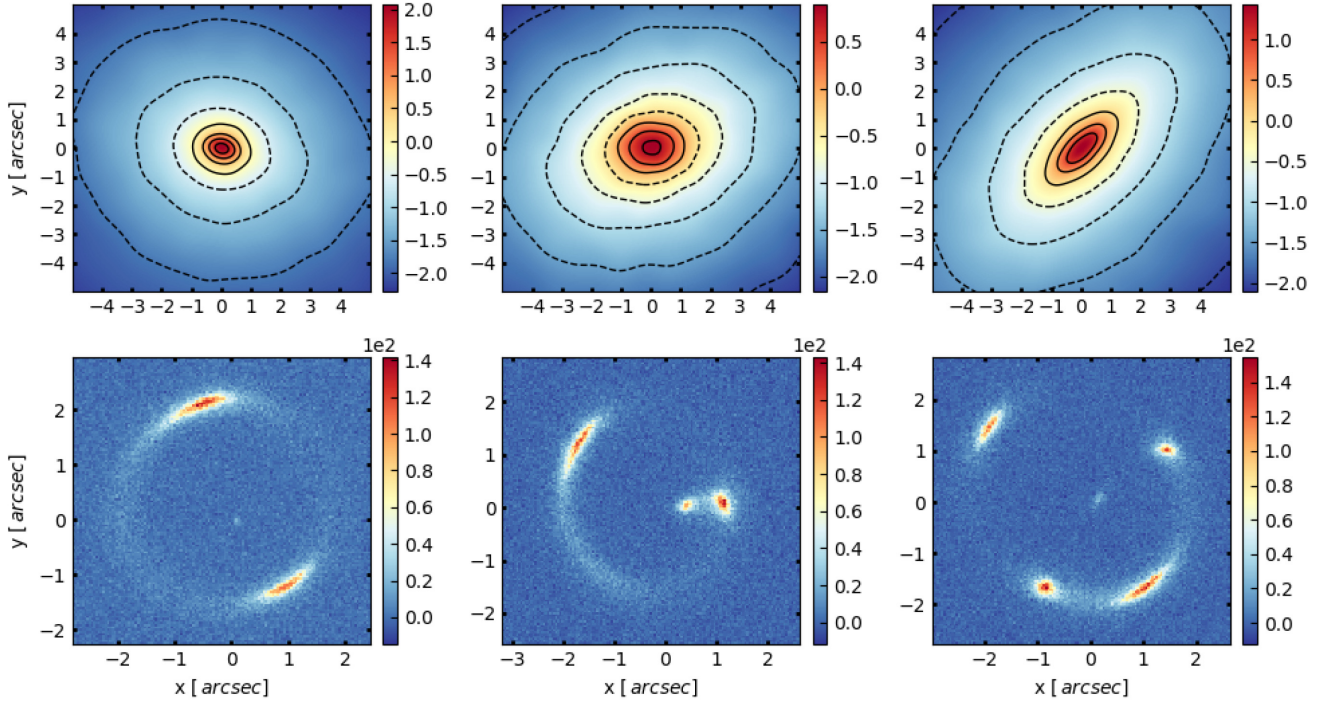


Figure 1. Top panels: The convergence maps of three representative galaxies selected from the Illustris-1 simulation. All substructures have been removed in these images. The dashed lines represent iso-convergence contours. Bottom panels: The corresponding mock lensing observations in our sample of lens systems.

$q, \theta, x_0, y_0, r_c, \gamma, \Gamma, \Gamma_\theta$). We use the FASTELL² library developed by Barkana (1998) to calculate deflection angles of non-isothermal ($\gamma \neq 2$) cored power laws.

3.1.3 Substructure

Each substructure is assumed to have a spherical NFW mass profile (Navarro, Frenk & White 1997) with a concentration given by the mass–concentration relation of Duffy et al. (2008) and a virial radius according to Bullock et al. (2001). We do not consider the effects of tidal truncation nor variations in the concentration–mass relation as a function of the distance from the host centre, as these are of secondary importance (see e.g. Despali et al. 2018). We assume the number density of substructure in mass bins of width $[m, m + dm]$ (i.e. the substructure mass function) to be well described by a power law (Springel et al. 2008):

$$\frac{dn^{\text{sub}}(m)}{dm} = n_0 \times m^{-\alpha}, \quad (4)$$

with a slope of $\alpha \approx 1.9$ and a normalization n_0 that depends in general on the redshift and the mass of the host galaxy (Gao et al. 2011; Xu et al. 2015). Here, we neglect both dependencies because the lens galaxies are all at the same redshift and span a narrow range in virial mass. The amplitude of the mass function is determined by the fraction of projected total mass of the host galaxy within the Einstein radius R_E (calculated according to Appendix A) contained in substructure, $f^{\text{sub}}(<R_E)$ (see Appendix B for a derivation). The number, masses, and projected positions of each substructure η^{sub} realization are a free nuisance parameter, while $f^{\text{sub}}(<R_E)$ is the main target parameter of the inference problem. In the following, we drop

the argument of $f^{\text{sub}}(<R_E)$ and write f^{sub} , while always referring to the fraction within the Einstein radius unless stated otherwise.

3.2 Reconstruction approach

In this section, we describe the statistical method we use to infer the macro-model parameters η^{macro} and the substructure mass fraction f^{sub} while marginalizing over the source surface brightness distribution and the substructure realizations.

3.2.1 Priors

For the parameters describing the lensing mass distribution, we choose the following priors: a uniform prior for the amplitude κ_0 , the axial ratio q , the angular orientation θ , and the slope γ , a Gaussian prior for the position x_0, y_0 and a lognormal distribution for the core radius r_c .

The tessellated source surface brightness distribution is drawn from a Gaussian regularizing prior:

$$\mathcal{P}(s|\mathbf{S}, \lambda) = \mathcal{G}(s, \lambda^{-1}\mathbf{S}), \quad (5)$$

where the matrix \mathbf{S} determines the form of the regularization and λ its strength. In particular, we choose a form of \mathbf{S} that penalizes either the gradient or the curvature at the vertices spanning the mesh (e.g. Suyu et al. 2006). We choose a log uniform prior on the regularization strength (e.g. Vegetti & Koopmans 2009a).

The probability of a substructure having a mass m in $[m, m + dm]$ is related to the mass function introduced in Section 3.1.3 via the following relation:

$$\mathcal{P}(m) = \frac{dn^{\text{sub}}}{dm} \bigg/ \int_{10^6 M_\odot}^{10^{10} M_\odot} dm \frac{dn^{\text{sub}}}{dm}. \quad (6)$$

²<http://wise-obs.tau.ac.il/~barkana/codes.html>

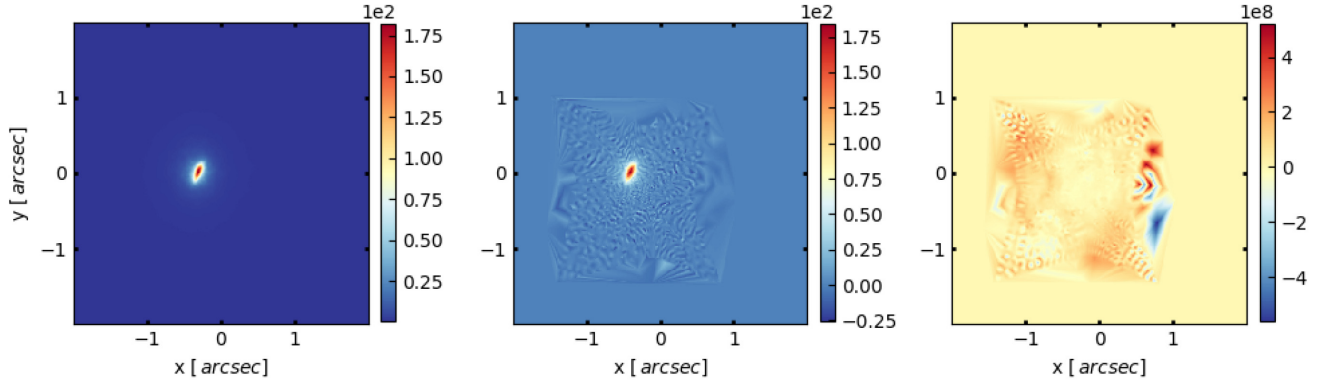


Figure 2. From left to right: The input source selected from the Illustris-1 simulation, the source inferred from the lens modelling of one of the lens systems in our sample, a prior sample of the surface brightness distribution. Notice that in the latter case the resulting field realization does not resemble a realistic source brightness distribution. The middle and right plots were generated using the same regularization form \mathbf{S} and strength λ .

We assume that the number of substructure N^{sub} follows a Poisson distribution

$$\mathcal{P}(N^{\text{sub}}|\mu) = \frac{e^{-\mu} \mu^{N^{\text{sub}}}}{N^{\text{sub}}!}, \quad (7)$$

of mean value μ given by

$$\mu = A^{\text{data}} \times \frac{f^{\text{sub}}(< R_E) \times \Sigma_{\text{crit}}}{< m >_{\mathcal{P}(\mathbf{m})}}, \quad (8)$$

where A^{data} is the area covered by the data (see Appendix B for a derivation). We assume a prior probability for the substructure projected positions which is uniform within the extent of the considered lens plane (Xu et al. 2015).

We choose a prior of $\mathcal{P}(f^{\text{sub}}) \propto (f^{\text{sub}})^{-1/2}$, which is the Jeffreys prior of the likelihood $\mathcal{P}(N^{\text{sub}}|f^{\text{sub}})$ (see Appendix C).

3.2.2 Macro-model reconstruction

In order to find the optimal macro-model parameters, we propose a modified version of ABC. ABC is usually motivated by inference problems, for which the Likelihood is not accessible. In Appendix D, we discuss why we follow this approach in this work and why the evaluation of the Likelihood poses a challenge for our analysis. In its simplest form, ABC is a rejection sampling algorithm in which prior samples of the target parameters – in this case samples of η^{macro} – are accepted/rejected according to the distance between the model realization they generate $\mathbf{b}(\mathbf{x})$ and the observed data $\mathbf{d}(\mathbf{x})$. Accepting the subset of samples closest to the real observation yields a set of samples approximating the posterior distribution. Accepting only perfect matches would yield the exact posterior distribution, although these are extremely unlikely for a finite number of realizations. Therefore, it is customary to set a distance threshold or accept only the fraction of the drawn samples that are closest to the data. Alternatively, one can compare statistical summaries $\Phi(\mathbf{b}(\mathbf{x}, \eta_i^{\text{macro}}))$ and $\Phi(\mathbf{d})$ rather than the mock data realizations and observations directly to each other. This approach improves the acceptance rate of the procedure, but only approximates the true posterior. As described below, the latter is the approach adopted in this paper.

A fully forward modelling method requires that we draw a realization of the source surface brightness distribution from a chosen prior (see Section 3.2.1). This requirement, together with the pixelated nature of our source, poses a challenge as every sampled

source brightness distribution is almost guaranteed to be far away from the true one as illustrated in Fig. 2. Searching through the parameter space of the target parameters η^{macro} while drawing new source realizations in every sample would, therefore, require a large number of samples, rendering the method infeasible. For this reason, we would like to obtain a distance measure that directly compares a lens configuration to the observations, without having to draw a source realization explicitly. We propose, therefore, to use the following Evidence as a proxy to a conventional distance measure:

$$\begin{aligned} \text{dist}(\mathbf{d}, \eta^{\text{macro}}) &\approx -2 \log \mathcal{P}(\mathbf{d}|\mathbf{L}, \lambda) \\ &= -2 \log \left[\int ds \, dn \mathcal{P}(\mathbf{d}|\mathbf{L}, s, \mathbf{n}) \mathcal{P}(s|\mathbf{S}, \lambda) \mathcal{P}(\mathbf{n}|\mathbf{N}) \right] \\ &= -2 \log [\mathcal{G}(\mathbf{d}, \mathbf{N} + \lambda^{-1} \mathbf{PLSL}^T \mathbf{P}^T)], \end{aligned} \quad (9)$$

where $\mathbf{L} = \mathbf{L}(\eta^{\text{macro}})$ is the lensing operator for a macro-model η^{macro} and \mathbf{P} a blurring matrix reproducing the effects of the PSF $p(\mathbf{x})$. In particular, since one can evaluate the integral analytically, it will also include the more realistic source configurations that are of interest in the inference. Sampling individual source realizations will, in contrast, tend to be far away from what is expected for real galaxies (as discussed in the previous section). Since the priors on the source and the noise are Gaussian distributions, the maximum-posterior source appears implicitly in the exponent of the posterior probability distribution.

Heuristically, we expect those lens configurations with higher Evidence to match the data more frequently than those with lower Evidence. Another, more Bayesian viewpoint is that the Evidence can be interpreted as a measure of credibility of the data \mathbf{d} on the hypothesis of a η_i^{macro} (see e.g. Cox 1946). Both arguments indicate that we should prefer to accept higher Evidence samples to obtain a posterior approximation. Following this consideration, we rank the drawn samples in order of their Evidence values and accept the fraction of samples with the highest values. In order to improve the convergence behaviour further, we introduce a proposal distribution $\mathcal{Q}(\eta^{\text{macro}})$, which we recursively update until it generates samples close to the posterior distribution.

Our inference on the macro-model parameters then proceeds in an iterative fashion as follows:

- (i) We draw N^{samp} samples of macro-model parameters η_i^{macro} from the proposal distribution. At the first iteration, we initialize the proposal distribution to match the prior introduced in Section 3.2.1, i.e. $\mathcal{Q}(\eta^{\text{macro}}) = \mathcal{P}(\eta^{\text{macro}})$.

(ii) For each sample, we calculate its importance sampling weight $w_i = \mathcal{P}(\eta_i^{\text{macro}})/Q(\eta_i^{\text{macro}})$ and Evidence $\mathcal{P}_i = \mathcal{P}(\mathbf{d}|L(\eta_i^{\text{macro}}))$. We accept the N^{acc} samples with the highest values of $\mathcal{P}_i \times w_i$ (see Appendix E for further details). Whenever we find that the effective number of samples

$$N^{\text{eff}} = \left(\sum_{i=1}^{N^{\text{samp}}} \mathcal{P}_i \times w_i \right)^2 / \left(\sum_{i=1}^{N^{\text{samp}}} \mathcal{P}_i^2 \times w_i^2 \right) \quad (10)$$

is higher than N^{acc} , we accept this effective number of samples instead. A chosen value of N^{acc} therefore determines the minimum relative acceptance threshold of $\epsilon = \frac{N^{\text{acc}}}{N^{\text{samp}}}$. The above acceptance strategy ensures that we do not underestimate the region within which we have to probe the parameter space in the following iteration.

(iii) We update the proposal distribution according to the following expression :

$$Q(\eta^{\text{macro}}) = q \times \mathcal{G}(\eta^{\text{macro}} - \mu, \Sigma) + (1 - q) \times \mathcal{P}(\eta^{\text{macro}}), \quad (11)$$

where $\mathcal{G}(\eta^{\text{macro}} - \mu, \Sigma)$ is a Gaussian distribution estimated from the accepted samples. Above, q determines the fraction of samples drawn from the prior versus the fraction drawn from the estimated Gaussian distribution. We set $q = 0.25$, so that one fourth of all drawn samples are used to search through the initial parameter space, thereby reducing the probability that we converge to a local minimum.

We repeat the steps (i)–(iii) N^{step} times, which results in a large number of samples, most of them drawn in the interesting regions of the parameter space. Following the discussion in Appendix E, the approximate posterior is given by the distribution of the accepted parameters:

$$\mathcal{P}^{\text{ABC}}(\eta^{\text{macro}}|\mathbf{d}) = \frac{1}{K^{\text{acc}}} \sum_{i \in \text{acc}} \delta^D(\eta^{\text{macro}} - \eta_i^{\text{macro}}), \quad (12)$$

with K^{acc} being the total number of accepted samples so far. The expectation value of some function $f(\eta^{\text{macro}})$ is then given by the average of the accepted samples, i.e.:

$$\begin{aligned} \langle f(\eta^{\text{macro}}) \rangle_{\mathcal{P}^{\text{ABC}}(\eta^{\text{macro}}|\mathbf{d})} &= \int d\eta^{\text{macro}} f(\eta^{\text{macro}}) \mathcal{P}^{\text{ABC}}(\eta^{\text{macro}}|\mathbf{d}) \\ &= \frac{1}{K^{\text{acc}}} \sum_{i \in \text{acc}} f(\eta_i^{\text{macro}}). \end{aligned} \quad (13)$$

For every lens we perform the above iterative scheme a total of three times, inferring the macro-model parameters or the source regularization level in an alternate fashion.

3.3 Substructure reconstruction

We now extend our inference to mass substructure within the lensing potential and the relative fraction f^{sub} . To this end, we include two additional steps where we first draw values of f^{sub} from its prior probability distribution $\mathcal{P}(f^{\text{sub}})$ and then draw explicit substructure realizations η^{sub} for each given value of f^{sub} . We draw only one substructure realization per macro-model. This is justified by the large number of draw samples, which ensures that for each pair $(\eta_i^{\text{macro}}, \eta_i^{\text{sub}})$ there exist another one $(\eta_j^{\text{macro}}, \eta_j^{\text{sub}})$ with a different substructure realization but similar macro-model parameters. For each macro-model and substructure combination, we then calculate the Evidence $\mathcal{P}_i = \mathcal{P}(\mathbf{d}|L(\eta_i^{\text{macro}}, \eta_i^{\text{sub}}))$ and follow the iterative scheme presented above.

In our approximate posterior, we would like to take into account that each substructure realization could also have been generated

from a mass function with a different f^{sub} than the one it has actually been drawn from. To this end, for each of these realizations we also calculate the probability of having been drawn from a model with \widehat{f}^{sub} and obtain the approximate posterior:

$$\mathcal{P}^{\text{ABC}}(f^{\text{sub}}|\mathbf{d}) = \frac{1}{K^{\text{acc}}} \sum_{i \in \text{acc}} v_i(f^{\text{sub}}), \quad (14)$$

where the interpolating function v_i is defined as

$$v_i(f^{\text{sub}}) = \frac{\mathcal{P}(N_i^{\text{sub}}|f^{\text{sub}})\mathcal{P}(f^{\text{sub}})}{\int d\widehat{f}^{\text{sub}} \mathcal{P}(N_i^{\text{sub}}|\widehat{f}^{\text{sub}})\mathcal{P}(\widehat{f}^{\text{sub}})}. \quad (15)$$

The generated substructure realizations will rarely match the one contained in the data. Rather than that, we expect that realizations drawn from the correct mass function will more often provide higher Evidence than those drawn from a different mass function, as the latter have either too few or too many substructures. If a particular substructure realization can reproduce the observed lensed images much better than any other, the weights introduced above will always ensure that more than a single value of f^{sub} will contribute to the posterior distribution. Using mock data with different level of f^{sub} , we have thoroughly tested our inference approach and found that we are able to recover the correct amount of mass in substructure with a precision that, as expected, depends on the number of lenses and the data quality.

Recently, Despali et al. (2018) have shown that low-mass haloes along the line of sight can significantly contribute to the number of detectable objects. For simplicity, here we focus only on the substructure contribution. However, our analysis can be easily extended to include both populations.

4 RESULTS

In this section, we present the results of the inference analysis described in Section 3.2 when applied to the sample of 24 mock lensing data presented in Section 2. In particular, for each lens, we create $N^{\text{step}} \times N^{\text{samp}} = 20 \times 4000$ lens configurations and choose $N^{\text{acc}} = 200$ at each step during the smooth modelling phase and $N^{\text{step}} \times N^{\text{samp}} = 40 \times 4000$ lens configurations and accept around half of them for the substructure inference.

4.1 Smooth modelling

4.1.1 Lensing mass distribution

A simple elliptical cored power-law mass distribution (with no substructure) can fit all of the mock observations to the noise level. Figs 3 and 4 show the best and the worst reconstructions, respectively. For the worst reconstruction, we find correlated image residuals at the 1.3σ level, which are related to the high dynamic range of the input lensed images that cannot be fully reproduced by the reconstructed source due to the effect of the regularization.

Even though we can accurately reproduce the lensed images to the noise level, we infer a lensing mass density distribution with a core that is much smaller than the true value. Gravitational lensing is mainly sensitive to the total mass within the Einstein radius and not its specific distribution. This means that it is insensitive to the presence of a core, when it does not directly affect the lensed images. As a result, the Illustris-1 galaxies in our sample have a core size of $r_c = 0.15\text{--}0.5$ arcsec, while the reconstructed cores tend to be of the order of $r_c = 5 \times 10^{-4}$ arcsec. As can be seen in the Figs 3 and 4, the relative difference in convergence between the simulated

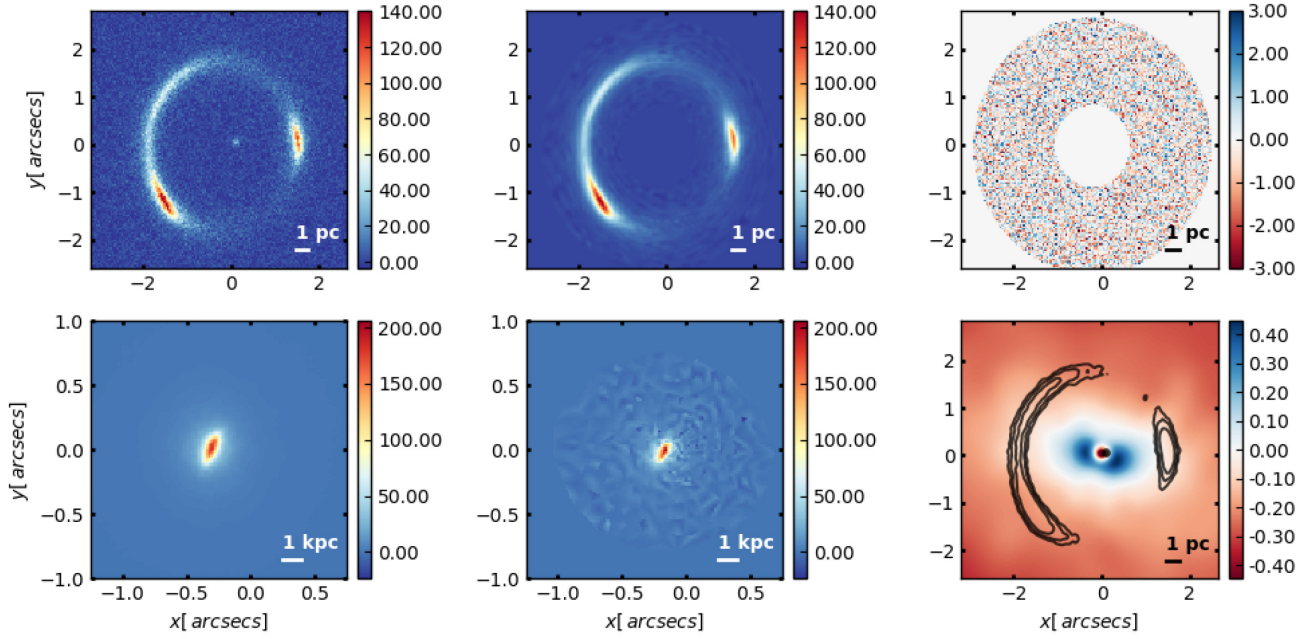


Figure 3. From left to right, top to bottom: The mock data $d(x) := I_{\text{gt}}(x)$, the reconstructed lensed images $I_{\text{rec}}(x)$, the image-plane residuals $r(x)$, the ground truth source $s_{\text{gt}}(x)$, the reconstructed source $s_{\text{rec}}(x)$, and the relative difference in convergence $\Delta\kappa/\kappa(x) = \kappa_{\text{gt}}(x)/\kappa_{\text{rec}}(x) - 1$.

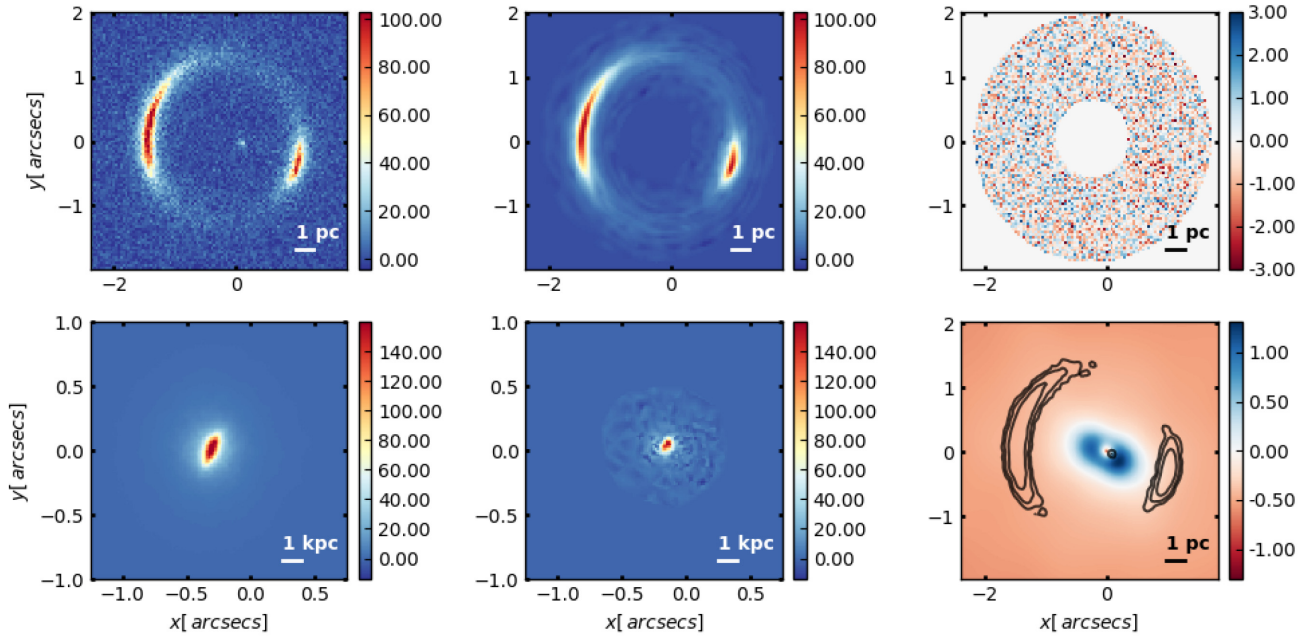


Figure 4. Same as Fig. 3 but for the mock with the highest residuals.

lenses and the power-law model stays constant over the extent of the lensed images, and hence can be compensated by a rescaling of the source size.

In order to further test the influence of the core we have also modelled one of the lens systems where the core directly affects the lensed images (e.g. the middle-bottom panel of Fig. 1) and found that in this case we can recover the correct core size within one standard deviation and obtain a source that is of the same size as the original one.

4.1.2 Source and time delay reconstruction

In general, we recover sources that tend to be on average 50 per cent more compact than the original ones, as reflected by a lack of power in their power spectra at large scales of $\mathcal{O}(\text{a few } kpc)$. Fig. 5 shows the power spectrum of the logarithmic convergence maps (top), the data (middle), and reconstructed model for the source (bottom); in all panels, we can compare the ground truth with the reconstructed model. This effect on the source size is in agreement with the findings by Ritondale et al. (in preparation) who have demonstrated,

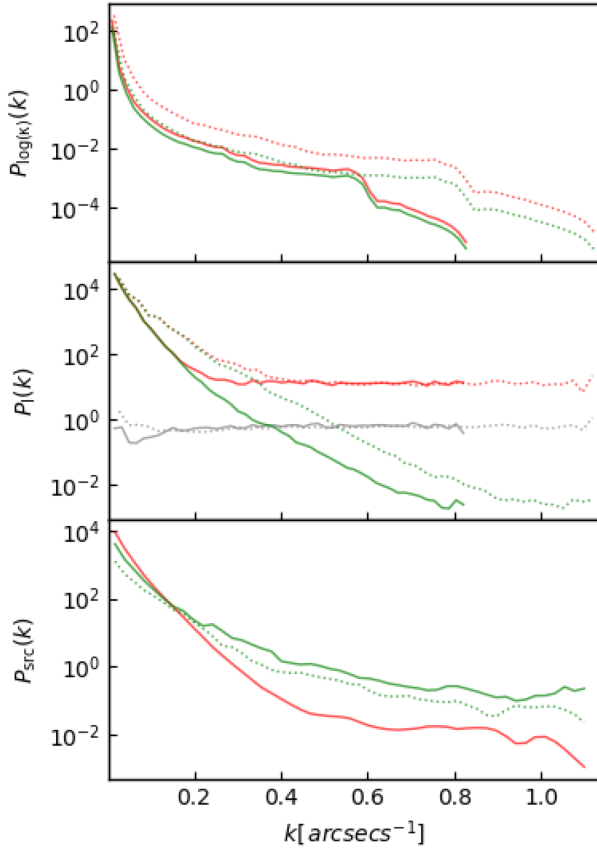


Figure 5. The top panel shows the power spectrum of the logarithmic convergence maps $\log(\kappa(x))$ for the groundtruth (red) and the model (green). The middle panel shows the power spectra of the data $d(x)$ (red), the reconstructed lensed images $I(x)$ (green), and the image plane residuals (grey). The bottom panel shows the power spectra of the groundtruth source (red) and the reconstructed one (green). All panels show the spectra for the mock data with the best (solid curve) and worst (dotted curve) reconstruction.

with the study of real gravitational lens systems, that a failure to fully capture the complexity of the lensing potential leads to a systematic error in the estimated morphological and physical properties of the reconstructed source by up to a factor of 22 per cent. In particular, we observe a correlation between the logarithm of $P_{\text{gt}}^{\log(\kappa)} / P_{\text{lens}}^{\log(\kappa)}(k) \forall k$ and the logarithm of $P_{\text{gt}}^s / P_{\text{lens}}^s(k)$ for $k = \mathcal{O}(\text{kpc})$ with a correlation coefficient $\rho \approx 0.95$ in our sample. Moreover, we find that the reconstructed sources show increased power at small scales with respect to the ground truth, which indicates a certain level of noise fitting, as also found by Bayer et al. (2018). A lognormal source prior may mitigate this issue significantly as it restricts the source brightness values to positive values. This potentially allows for reconstructing sources up to smaller scales and increase the sensitivity to substructures as a result.

We further consider the time delays of the reconstructed lens models. Following the discussion by Kochanek (2020), we calculate for each of the lens systems the expected fractional error on H_0 using the (mean) convergence at the Einstein radius $\kappa(R_E)$, i.e. $f_{H_0} = \frac{H_0^{gt}}{H_0^{\text{rec}}} - 1 = \frac{1 - \kappa_E^{gt}(R_E)}{1 - \kappa_E^{\text{rec}}(R_E)} - 1 = \frac{\Delta \kappa_E^{gt}}{\Delta \kappa_E^{\text{rec}}} - 1$, where κ_E^{gt} is the ground truth convergence used to generate data, i.e. the Illustris galaxies (see Section 2) or the control sample (see Section 4.2), while κ^{rec} is the convergence at the Einstein radius obtained from the lens modelling of these two samples. We find a median and 1σ percentiles of $f_{H_0} = 25^{+37}_{-19}$

per cent and $f_{H_0} = 12^{+6}_{-3}$ per cent, for the Illustris galaxies and the control sample, respectively. In both cases, the Hubble constant is, therefore, systematically underestimated. Notice, that our analysis uses as constraints on the mass distribution the extended lensed images only, while cosmographic analyses (see e.g. Suyu et al. 2010; Chen et al. 2019), also make use of the additional information provided by the kinematics of the lens galaxy and the positions of quadruply-lensed quasars.

4.2 Substructure reconstruction

We now allow for the presence of substructure in the lens modelling to infer the amount of lens galaxy mass in substructures, f^{sub} .

To validate this inference, we generate a control sample of 24 lens systems with the same observational properties (i.e. signal-to-noise ratio and angular resolution) as our Illustris-1 sample. To this end, we use as input lensed images those corresponding to the highest evidence macro-model obtained in the previous section by modelling the Illustris-1 galaxies with a smooth power law. This approach provides us with a sample for which we have a perfect knowledge of the lensing potential. We model both the mocks generated directly with the Illustris-1 galaxies and the control sample. As the input data in both samples do not contain any substructure, we expect the control sample to lead to an inferred value of f^{sub} consistent with zero. Any potential difference in f^{sub} between the two samples can be then attributed to the additional complexity of the Illustris-1 galaxies.

Fig. 6 shows the joint posterior on f^{sub} for the Illustris-1 (solid line) and the control sample (dashed line). Furthermore, it shows the ABC Likelihood of f^{sub} for one of the Illustris-1 galaxies in three projections (coloured lines). For small values of f^{sub} , the Likelihood is flat as the number of substructures affecting the lensed surface brightness approaches zero. This flattening may appear before the point where no substructures are placed due to the sensitivity of the data. Within the region where the Likelihood is flat, the posterior inherits the shape of the prior. For large values of f^{sub} , the Likelihood decreases, reflecting an overabundance of substructures that is not compatible with the data.

From the analysis of all gravitational lens systems in each of the two samples, we find a posterior upper limit of $f^{\text{sub}} \leq 1.7 \times 10^{-3}$ and $f^{\text{sub}} \leq 2 \times 10^{-3}$ at the 68 per cent confidence level for the Illustris-1 and the control sample, respectively. The inferred f^{sub} from the two samples agree with each other within the uncertainty arising from the finite number of samples of $(\eta^{\text{macro}}, \eta^{\text{sub}})$ drawn in the analysis. In both cases, the posterior upper limits differ significantly from the prior upper limit of $f^{\text{sub}} \leq 4.7 \times 10^{-2}$. Both samples are compatible with the Null-Hypothesis that the lensing potential does not contain any substructures, i.e. $f^{\text{sub}} = 0$. We conclude, therefore, that baryonic structure, as well as small-scale complexity, do not have a significant impact on our capability of correctly inferring the amount of substructure. We find that the sources do not change much with respect to the case without substructure. In order to test the effect of our choice for the input source galaxy, we repeat the analysis using *HST* observations of a local galaxy and find no significant change on the inferred upper limit on f^{sub} .

Recently, from the analysis of flux-ratio anomalies in multiply imaged quasars lensed by elliptical galaxies from the Illustris-1 simulation with the same smoothing level, Hsueh et al. (2018) have found that baryonic components in the lensing galaxies are responsible for an increase in the probability of flux-ratio anomalies by 8 per cent. Similarly, Gilman et al. (2017) have concluded

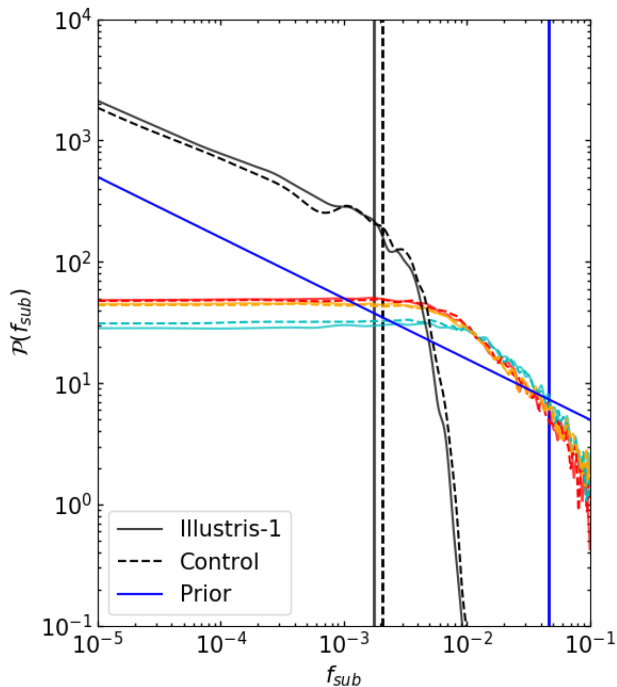


Figure 6. The posterior distribution of f_{sub} for the Illustris-1 sample (continuous curve) and the control sample (dashed curve). Furthermore, we show the Likelihood for one of the Illustris-1 lens galaxies, and show the behaviour for all three projections (red, orange, and cyan). We find that the upper confidence limits of f_{sub} do not change much between the mock and the control samples (in particular when comparing the reconstructions on the level of individual lens systems). The prior probability distribution of f_{sub} is shown in blue. The vertical lines indicate the 68 per cent confidence levels (CL) of the prior and posterior distributions for the mock and the control sample, respectively.

that 10 per cent of the flux-ratio anomalies in elliptical galaxies can be attributed to baryonic structures in their analysis of mock data based on real *HST* observations. Both results have important implications for the quantification of sub- and line-of-sight structure with gravitationally lensed quasars. We attribute the difference from our findings to the fact that flux ratios are sensitive to the second derivative of the lensing potential rather than the first, and are therefore more affected by general departures from simple smooth distributions. As the sensitivity of extended arcs and rings is strongly dependent on the angular resolution of the data, we expect our results to change with increasing data quality.

On the other hand, our results are also in disagreement with Vegetti et al. (2014) and Ritondale et al. (in preparation), who from the analysis of real lens systems with a similar data quality as ours, have identified the presence of complex mass components that are degenerate with the presence of a large population of substructure and can lead to false detections. This discrepancy seems to indicate that galaxies in the Illustris-1 simulations are smoother than real galaxies and that their level of complexity at scales that we can resolve – i.e. scales $> \mathcal{O}(kpc)$ – is such that it has a negligible lensing effect which is easily absorbed by changes in the macro-model and the source structure. It should also be considered that the simulated galaxies analysed here were chosen to match the global properties of known lenses, but unlike the latter they have not been selected based on their spectral properties. This may potentially lead to a sample of simulated lens galaxies that is more homogeneous and more regular than real ones. We therefore conclude that higher-

resolution simulations together with more realistic selection criteria are key to properly characterize their central mass distribution in a way that is not affected by the presence of an un-physical core and investigate the level of complexity in more realistic galaxies and its effect on the detection of low-mass haloes.

5 SUMMARY AND CONCLUSIONS

Using a novel Bayesian forward modelling technique based on ABC, we have analysed a sample of mock lensing observations generated from a simulated source and lensing potentials taken from the Illustris-1 simulation. Our results have interesting implications for a variety of measurements, from the study of lensed galaxies to constraints on cosmology and dark matter. We summarize them as follows:

(i) Our capability of reproducing the lensed images down to the noise level without fully correctly modelling the cored central mass density distribution of the lenses indicates some form of the source-position transformation (SPT; Schneider & Sluse 2014), in line with the previous findings by Unruh et al. (2017). As a consequence, our reconstructions lead to a *systematic* fractional error on the Hubble constant of 25^{+37}_{-19} per cent (in comparison to a *static* error of 12^{+6}_{-3} per cent when the shape of the lensing potential is perfectly known). This result is in agreement with the latest analysis of Blum, Castorina & Simonović (2020) that shows that cored (dark matter) mass density distributions give rise to approximate MSDs, and an error on the inferred Hubble constant. The latest cosmographic analyses (see e.g. Wong et al. 2019) have attempted to break these degeneracies by including the information contained in the kinematic properties of the lens galaxies and the positions of the lensed quasar images. However, the validity of this approach has been recently debated by Kochanek (2020), who has demonstrated that departures from single power-law mass distributions are responsible for a fractional error on the Hubble constant of 30 per cent. While the cores in the simulations analysed in this paper are artefacts related to limited resolution, cored mass density distribution in real galaxies may be developed by the effect of baryonic processes (see e.g. Chan et al. 2015) or changes in the dark matter properties (Schive, Chiueh & Broadhurst 2014; Spergel & Steinhardt 2000). Moreover, similar additional complexities exist in real galaxies are related, for example, to the presence of faint discs (Hsueh et al. 2018), bars, or other (baryonic) structures (Gilman et al. 2018; Xu et al. 2013). More generally, there exist many plausible deviations from a smooth power-law distribution, such as broken power laws (see e.g. Du et al. 2020) or multiple component models (see e.g. Nightingale, Dye & Massey 2018), which can produce comparable degeneracies. Together with the findings of Blum et al. (2020), our results have important implications for the analysis of time delays and a potential solution to the H_0 tension (Wong et al. 2019).

(ii) The MSD we encounter in this work further affects the reconstruction of the sources, for which we underestimate the size by 50 per cent on average. This finding is in agreement with Ritondale et al. (in preparation), who showed for a Ly α -emitting galaxy of the BELLS GALLERY that a correct modelling of the complex lensing potential is essential to reconstruct the properties of the lensed galaxy. In particular, they find that mass components beyond the simple power-law model, in the form of pixelated potential corrections, are required for correct focusing of the source. The reconstructed sources also differ from the input source on small scales, reflecting the presence of noise in the data and the choice of a Gaussian regularising prior. We expect that a lognormal prior

or a hyper-prior as in Rizzo et al. (2018) may provide more stable results as well as a better sensitivity to low-mass haloes by reducing the freedom of the source structure to re-absorb the effect of the latter on the lensed images.

(iii) We find no degeneracy between complex structures in the lensing potential and low-mass substructures. After having removed all substructures from the simulations, we have inferred a fraction of mass in substructure which is consistent with the absence of any substructure and with what was derived from a control sample for which we have a perfect knowledge of the lensing potential. This is in disagreement with Ritondale et al. (2019), Xu et al. (2015), and Gilman et al. (2019), who have shown both with numerical simulations and observations that un-modelled small-scale structures in the lensing mass distribution can lead to significant flux-ratio and surface-brightness anomalies. We believe the origin of this discrepancy to lie partly on the limited resolution of the simulations and partly on the selection criteria adopted in this work, as well as a different sensitivity of lensed quasars to changes in the potential.

What is important to notice is that a simple power-law model provides a good fit to the lensing observable. Meaning that the quality of fit is not a good measure to exclude the potential presence of un-modelled mass components. In line with previous works, our results underlines the importance of complex lensing mass distributions that go beyond the standard power-law assumptions as well as the need of extra information (e.g. from stellar kinematics or time delays Barnabè & Koopmans 2007; Schneider & Sluse 2014) to break existing degeneracies. From a numerical perspective, our work shows the importance of higher resolution and more realistic numerical simulations to further quantify potential systematic effects in strong gravitational lensing reconstructions.

ACKNOWLEDGEMENTS

We thank Matt Auger, Mohammadreza Ayromlou, Francesca Rizzo, Elisa Ritondale, Devon Powell, Jens Jasche, Sampath Mukherjee, Matteo Frigo, Simon Birrer, and Daniel Gilman for insightful discussions. S.V. has received funding from the European Research Council (ERC) under the European Union's Horizon 2020 research and innovation programme (grant agreement no. 758853). J-WH acknowledges support from the Netherlands Organization for Scientific Research (NWO) (Project No. 629.001.023) and the Chinese Academy of Sciences (CAS) (Project No. 114A11KYSB20170054). We also want to thank the Illustris-Collaboration for making their data publically available.

REFERENCES

Akeret J., Refregier A., Amara A., Seehars S., Hasner C., 2015, *J. Cosmol. Astropart. Phys.*, 2015, 043
 Barkana R., 1998, *ApJ*, 502, 531
 Barnabè M., Koopmans L. V. E., 2007, *ApJ*, 666, 726
 Bayer D., Chatterjee S., Koopmans L. V. E., Vegetti S., McKean J. P., Treu T., Fassnacht C. D., 2018, preprint ([arXiv:1803.05952](https://arxiv.org/abs/1803.05952))
 Birrer S., Amara A., Refregier A., 2017, *J. Cosmol. Astropart. Phys.*, 2017, 037
 Blum K., Castorina E., Simonović M., 2020, *ApJ*, 892, L27
 Bolton A. S., Burles S., Koopmans L. V. E., Treu T., Moustakas L. A., 2006, *ApJ*, 638, 703
 Brewer B. J., Huijser D., Lewis G. F., 2015, *MNRAS*, 455, 1819
 Bullock J. S., Kolatt T. S., Sigad Y., Somerville R. S., Kravtsov A. V., Klypin A. A., Primack J. R., Dekel A., 2001, *MNRAS*, 321, 559

Chan T. K., Kereš D., Oñorbe J., Hopkins P. F., Muratov A. L., Faucher-Giguère C.-A., Quataert E., 2015, *MNRAS*, 454, 2981
 Chen G. C.-F. et al., 2019, *MNRAS*, 490, 1743
 Cox R. T., 1946, *Am. J. Phys.*, 14, 1
 Daylan T., Cyr-Racine F.-Y., Rivero A. D., Dvorkin C., Finkbeiner D. P., 2018, *ApJ*, 854, 141
 Despali G., Vegetti S., 2017, *MNRAS*, 469, 1997
 Despali G., Vegetti S., White S. D. M., Giocoli C., van den Bosch F. C., 2018, *MNRAS*, 475, 5424
 Du W., Zhao G.-B., Fan Z., Shu Y., Li R., Mao S., 2020, *ApJ*, 892, 62
 Duffy A. R., Schaye J., Kay S. T., Dalla Vecchia C., 2008, *MNRAS*, 390, L64
 Falco E. E., Gorenstein M. V., Shapiro I. I., 1985, *ApJ*, 289, L1
 Gao L., Frenk C. S., Boylan-Kolchin M., Jenkins A., Springel V., White S. D. M., 2011, *MNRAS*, 410, 2309
 Genel S., Fall S. M., Hernquist L., Vogelsberger M., Snyder G. F., Rodriguez-Gomez V., Sijacki D., Springel V., 2015, *ApJ*, 804, L40
 Gilman D., Agnello A., Treu T., Keeton C. R., Nierenberg A. M., 2017, *MNRAS*, 467, 3970
 Gilman D., Birrer S., Treu T., Keeton C. R., Nierenberg A., 2018, *MNRAS*, 481, 819
 Gilman D., Birrer S., Treu T., Nierenberg A., Benson A., 2019, *MNRAS*, 487, 5721
 Hezaveh Y. D. et al., 2016, *ApJ*, 823, 37
 Hinshaw G. et al., 2013, *ApJS*, 208, 19
 Hsueh J.-W., Despali G., Vegetti S., Xu D. A., Fassnacht C. D., Metcalf R. B., 2018, *MNRAS*, 475, 2438
 Hsueh J.-W., Enzi W., Vegetti S., Auger M., Fassnacht C. D., Despali G., Koopmans L. V. E., McKean J. P., 2019, *MNRAS*, 492, 3047
 Hsueh J. W. et al., 2017, *MNRAS*, 469, 3713
 Hsueh J. W., Fassnacht C. D., Vegetti S., McKean J. P., Spingola C., Auger M. W., Koopmans L. V. E., Lagattuta D. J., 2016, *MNRAS*, 463, L51
 Jeffreys H., 1946, *Proc. R. Soc. London Ser. A*, 186, 453
 Kochanek C. S., 2020, *MNRAS*, 493, 1723
 Koopmans L. V. E., 2005, *MNRAS*, 363, 1136
 Kormann R., Schneider P., Bartelmann M., 1994, *A&A*, 284, 285
 Mao S., Schneider P., 1998, *MNRAS*, 295, 587
 Metcalf R. B., Petkova M., 2014, *MNRAS*, 445, 1942
 Möller O., Hewett P., Blain A. W., 2003, *MNRAS*, 345, 1
 Mukherjee S. et al., 2018, *MNRAS*, 479, 4108
 Navarro J. F., Frenk C. S., White S. D. M., 1997, *ApJ*, 490, 493
 Nelson D. et al., 2015, *Astronomy and Computing*, 13, 12
 Nierenberg A. M., Treu T., Wright S. A., Fassnacht C. D., Auger M. W., 2014, *MNRAS*, 442, 2434
 Nightingale J. W., Dye S., Massey R. J., 2018, *MNRAS*, 478, 4738
 Petkova M., Metcalf R. B., Giocoli C., 2014, *MNRAS*, 445, 1954
 Ritondale E., Vegetti S., Despali G., Auger M. W., Koopmans L. V. E., McKean J. P., 2019, *MNRAS*, 485, 2179
 Rizzo F., Vegetti S., Fraternali F., Di Teodoro E., 2018, *MNRAS*, 481, 5606
 Rybak M., Vegetti S., McKean J. P., Andreani P., White S. D. M., 2015, *MNRAS*, 453, L26
 Schaye J. et al., 2015, *MNRAS*, 446, 521
 Schive H.-Y., Chiueh T., Broadhurst T., 2014, *Nat. Phys.*, 10, 496
 Schneider P., Sluse D., 2014, *A&A*, 564, A103
 Shirazi M., Vegetti S., Nesvadba N., Allam S., Brinchmann J., Tucker D., 2014, *MNRAS*, 440, 2201
 Spergel D. N., Steinhardt P. J., 2000, *Phys. Rev. Lett.*, 84, 3760
 Spingola C., McKean J. P., Massari D., Koopmans L. V. E., 2019, *A&A*, 630, A108
 Springel V. et al., 2008, *MNRAS*, 391, 1685
 Springel V., 2010, *MNRAS*, 401, 791
 Springel V., White S. D. M., Tormen G., Kauffmann G., 2001, *MNRAS*, 328, 726
 Suyu S. H., Marshall P. J., Hobson M. P., Blandford R. D., 2006, *MNRAS*, 371, 983
 Suyu S. H., Marshall P. J., Auger M. W., Hilbert S., Blandford R. D., Koopmans L. V. E., Fassnacht C. D., Treu T., 2010, *ApJ*, 711, 201

- Teklu A. F., Remus R.-S., Dolag K., Beck A. M., Burkert A., Schmidt A. S., Schulze F., Steinborn L. K., 2015, *ApJ*, 812, 29
- Treu T., 2010, *ARA&A*, 48, 87
- Unruh S., Schneider P., Sluse D., 2017, *A&A*, 601, A77
- Vegetti S., Koopmans L. V. E., 2009a, *MNRAS*, 392, 945
- Vegetti S., Koopmans L. V. E., 2009b, *MNRAS*, 400, 1583
- Vegetti S., Koopmans L. V. E., Bolton A., Treu T., Gavazzi R., 2010, *MNRAS*, 408, 1969
- Vegetti S., Lagattuta D. J., McKean J. P., Auger M. W., Fassnacht C. D., Koopmans L. V. E., 2012, *Nature*, 481, 341
- Vegetti S., Koopmans L. V. E., Auger M. W., Treu T., Bolton A. S., 2014, *MNRAS*, 442, 2017
- Vogelsberger M. et al., 2014, *MNRAS*, 444, 1518
- Wong K. C. et al., 2019, preprint (arXiv:1907.04869)
- Xu D., Sluse D., Gao L., Wang J., Frenk C., Mao S., Schneider P., Springel V., 2015, *MNRAS*, 447, 3189
- Xu D., Springel V., Sluse D., Schneider P., Sonnenfeld A., Nelson D., Vogelsberger M., Hernquist L., 2017, *MNRAS*, 469, 1824
- Xu D. D., Sluse D., Gao L., Wang J., Frenk C., Mao S., Schneider P., 2013, preprint (arXiv:1307.4220)

APPENDIX A: THE EINSTEIN RADIUS

The Einstein radius R_E is defined as the radius of a circle within which the average mass density is given by the critical density:

$$M(< R_E) = A(< R_E) \times \Sigma_{\text{crit}} = \pi R_E^2 \times \Sigma_{\text{crit}}. \quad (\text{A1})$$

In this case, it is straightforward to calculate the mass within the Einstein radius by integrating the parametrized convergence within the circle and multiplying it by Σ_{crit} . Solving the resulting equation for R_E yields a definition of the Einstein radius in the chosen parametrization of the convergence. In order to obtain the elliptical Einstein radius, we consider the rescaled radius $R_E \rightarrow \tilde{R}_E = R_E/\sqrt{q}$, so that

$$M(< \tilde{R}_E) = \pi \tilde{R}_E^2 \times \Sigma_{\text{crit}}, \quad (\text{A2})$$

which is consistent with the previous definition for $q = 1$. For the parametrized version of the macro-model used in this work, we determine the mass within $\tilde{R}_E = R_E/\sqrt{q}$ as

$$\begin{aligned} M(< R_E/\sqrt{q}) &= \Sigma_{\text{crit}} \int_0^{2\pi} d\theta \int_0^{R_E/\sqrt{q}} d\rho \, q \rho \times \kappa^{\text{macro}}(\rho) \\ &= \Sigma_{\text{crit}} 2\pi \int_0^{R_E/\sqrt{q}} d\rho \, q \rho \times \frac{\kappa_0 (2 - \frac{\gamma}{2}) q^{-1/2}}{2(r_c^2 + \rho^2)^{(\gamma-1)/2}} \\ &= \Sigma_{\text{crit}} \pi \times \frac{\frac{1}{2} (2 - \frac{\gamma}{2})}{(3 - \gamma)/2} \frac{\kappa_0 q^{1/2}}{(r_c^2 + \rho^2)^{(\gamma-3)/2}} \Big|_{\rho=0}^{\rho=R_E/\sqrt{q}} \\ &= \Sigma_{\text{crit}} \pi \times \kappa_0 \frac{(2 - \frac{\gamma}{2})}{(3 - \gamma)} q^{1/2} \\ &\quad \times \left[(r_c^2 + R_E^2/q)^{(3-\gamma)/2} - (r_c^2)^{(3-\gamma)/2} \right]. \quad (\text{A3}) \end{aligned}$$

The Einstein radius R_E for a given set of macro-model parameters is then

$$R_E^2 = \frac{\kappa_0 (4 - \gamma)}{2 (3 - \gamma)} q^{1/2} \left[(r_c^2 + R_E^2/q)^{(3-\gamma)/2} - (r_c^2)^{(3-\gamma)/2} \right]. \quad (\text{A4})$$

For $r_c = 0$, this definition of the Einstein radius matches the one described by Vegetti et al. (2014):

$$R_E^{\gamma-1} = \frac{\kappa_0 (4 - \gamma)}{2 (3 - \gamma)} q^{(\gamma-2)/2}. \quad (\text{A5})$$

It further reduces to the definition by Kormann, Schneider & Bartelmann (1994) in the isothermal case, where $\gamma = 2$, i.e. $R_E = \kappa_0$.

APPENDIX B: MASS FUNCTION NORMALIZATION AND MEAN NUMBER OF SUBSTRUCTURES

In this Appendix, we describe the derivation of the mass function normalization constant from the condition that we have an average fraction of mass contained in substructures within the Einstein radius $f^{\text{sub}}(< R_E)$. This condition can be written explicitly as

$$\begin{aligned} f^{\text{sub}}(< R_E) &= \left\langle \frac{\sum_{k=1}^{N^{\text{sub}}} m_k}{M(< R_E)} \right\rangle_{\mathcal{P}(N^{\text{sub}}, < R_E)} \\ &= \frac{\mu(< R_E) < m > \mathcal{P}(m)}{M(< R_E)}, \quad (\text{B1}) \end{aligned}$$

where $\mu(< R_E)$ is the mean number of objects within the Einstein radius and $< m > \mathcal{P}(m)$ is the average mass of a substructure. $\mathcal{P}(N^{\text{sub}}, \{m_k, \rho_k\})$ is the probability distribution associated with a substructure realization with N^{sub} clumps, each with their respective mass m_k and radial position ρ_k .

The amplitude of the mass function n_0 can be determined by requiring that $\mu(< R_E)$ matches the definition given in equation (B1), i.e.:

$$\mu(< R_E) = A(< R_E) \times \int_{10^6 M_\odot}^{10^{10} M_\odot} dm \frac{dn^{\text{sub}}}{dm}. \quad (\text{B2})$$

Using the above definition for the Einstein radius, the proportionality constant in equation (4) is

$$n_0 = \frac{f^{\text{sub}}(< R_E) \times \Sigma_{\text{crit}}}{< m > \mathcal{P}(m) \times \int_{10^6 M_\odot}^{10^{10} M_\odot} dm m^{-\alpha}}. \quad (\text{B3})$$

We assume that the density of substructures is constant throughout the extensions of the mock observation. In order to obtain the mean number of objects μ in the considered area, we integrate the mass function over m and multiply it with the area A^{data} covered by the mock observation:

$$\begin{aligned} \mu &= A^{\text{data}} \times \int_{10^6 M_\odot}^{10^{10} M_\odot} dm \frac{dn^{\text{sub}}}{dm} \\ &= A^{\text{data}} \times \frac{f^{\text{sub}}(< R_E) \times \Sigma_{\text{crit}}}{< m > \mathcal{P}(m)}. \quad (\text{B4}) \end{aligned}$$

APPENDIX C: JEFFREYS' PRIOR

For the inference task of the free parameter, f^{sub} the Jeffreys' prior (Jeffreys 1946) would require us to consider the full Likelihood function $\mathcal{P}(\mathbf{d}|\mu)$ and marginalize it over the space data realizations. As this is computationally prohibited, we consider the Jeffreys' prior of the probability density $\mathcal{P}(N^{\text{sub}}|\mu)$, which being a Poisson distribution, leads to a prior of $\mathcal{P}(f^{\text{sub}}) \propto (f^{\text{sub}})^{-1/2}$. We expect this simplified prior distribution to remain non-informative for our reconstruction process. Moreover, it has the advantage of being integrable under the assumption of a finite upper limit on f^{sub} and allows us to correctly probe a parameter that may vary by several orders of magnitude. We choose a range of $f^{\text{sub}} \in [10^{-6}, 10^{-1}]$, which includes the case that $\mu(f^{\text{sub}}) + \sqrt{\mu(f^{\text{sub}})} < 1$, i.e. that there are no substructures within one standard deviation of the Poisson distribution $\mathcal{P}(N^{\text{sub}}|\mu)$.

APPENDIX D: MOTIVATING AN ABC APPROACH

One of the main goals of this work is the reconstruction mass function parameters. The likelihood of this problem under the model assumptions specified in Section 3 is

$$\begin{aligned} \mathcal{P}(\mathbf{d}|\{f_{\text{sub}}, m_{\text{hm}}\}) \\ = \sum_{N^{\text{sub}}=0}^{\infty} \left(\prod_{n=1}^{N^{\text{sub}}} \int dm_n \int d\mathbf{x}_n \mathcal{P}(m_n, \mathbf{x}_n|\{f_{\text{sub}}, m_{\text{hm}}\}) \right) \\ \times \mathcal{P}(N^{\text{sub}}|\{f_{\text{sub}}, m_{\text{hm}}\}) \\ \times \mathcal{P}\left(\mathbf{d}|\mathbf{L}\left(\eta^{\text{macro}}, \{\mathbf{x}_n, m_n\}_{n=1}^{N^{\text{sub}}}\right)\right). \end{aligned} \quad (\text{D1})$$

While we can analytically calculate the last factor of this product [corresponding to equation (9) once $\mathbf{L}(\eta^{\text{macro}}, \eta^{\text{sub}} := \{\mathbf{x}_n, m_n\}_{n=1}^{N^{\text{sub}}}]$ is given, the combination with the integrals over positions \mathbf{x}_n and masses m_n as well as the summation over N^{sub} pose a challenge for analytical evaluation.

In order to evaluate expression (D1), one may follow a reversible jump MCMC approach as done by Brewer, Huijser & Lewis (2015) or Daylan et al. (2018). However, these methods usually require to reduce the parameters in the model, for example, by switching to a parametric source rather than a free form surface brightness field. Furthermore, these approaches tend to be computationally expensive.

Another way is to marginalize over the substructure realizations rigorously. Hsueh et al. (2019) follow this approach and explicitly integrate over $\mathcal{O}(10^6)$ substructure realizations per M_{hm} value in their regular grid of mass function parameters. In this case, the flux-ratio analysis benefits from the small number of observables, i.e. $\dim(\mathbf{d}) \approx \mathcal{O}(10)$. The evaluation of the analogous function to equation (9) is therefore much faster than in the case of extended arcs with $\dim(\mathbf{d}) \approx \mathcal{O}(100^2)$. Notice that the computational cost of expression D1 would increase even further with the inclusion of line-of-sight haloes, which constitute a possible extension of the model used in this work.

Given that our goal is to keep the physical model as general as possible that we can generate substructure realizations with forward modelling, and that for a (somewhat) limited number of samples one will obtain conservative results with ABC, we decided to follow this approach.

APPENDIX E: IMPORTANCE SAMPLING AND WEIGHTING OF SAMPLES

Standard importance sampling uses weights w_i and applies them to the samples that approximate the posterior distribution:

$$\mathcal{P}(\eta^{\text{macro}}|\mathbf{d}) = \frac{1}{K_{\text{acc}}} \sum_{i \in \text{acc}} \delta^D(\eta^{\text{macro}} - \eta_i^{\text{macro}}) \times w_i, \quad (\text{E1})$$

However, in our implementation, as expressed by equation (12), we do not include any weight, as this is done implicitly by the acceptance strategy. In order to justify this, we consider the following relation:

$$\begin{aligned} \mathcal{P}(\mathbf{x}|\mathbf{d}) &= \frac{\mathcal{P}(\mathbf{d}|\mathbf{x})}{\mathcal{P}(\mathbf{d})} \mathcal{P}(\mathbf{x}) \\ &= \frac{\mathcal{P}(\mathbf{d}|\mathbf{x})}{\mathcal{P}(\mathbf{d})} \frac{\mathcal{P}(\mathbf{x})}{Q(\mathbf{x})} Q(\mathbf{x}) = \frac{\tilde{\mathcal{P}}(\mathbf{d}|\mathbf{x})}{\mathcal{P}(\mathbf{d})} Q(\mathbf{x}), \end{aligned} \quad (\text{E2})$$

with $\tilde{\mathcal{P}}(\mathbf{d}|\mathbf{x}) = \mathcal{P}(\mathbf{d}|\mathbf{x}) \frac{\mathcal{P}(\mathbf{x})}{Q(\mathbf{x})}$. This relation implies that one can interpret the importance sampling as a change in the Likelihood³ and the prior in such a way that their changes cancel each other out.

As we use the $\mathcal{P}(\mathbf{d}|\mathbf{x})$ as our distance measure, we include the weight in the distance that decides whether or not a sample gets accepted rather than multiplying the weight to the corresponding sample. In doing so, we free ourselves from accounting for sample weights at the price of the caveat that the posterior distribution of the importance sampled parameters tend to resemble the shape of the proposal distribution.

In our case, we apply importance sampling on the macro-model parameters η^{macro} , for which previous tests have shown that their posteriors closely resemble Gaussian distributions, therefore justifying our choice of the proposal distribution. In order to improve the approximation, one could use Gaussian mixture models instead of a single Gaussian distribution to describe the proposition distribution. This form of the proposal distribution would allow one to account for more general shapes of posteriors.

³Which we refer to as evidence in this paper, as it is the evidence in the case of source reconstruction.

This paper has been typeset from a \LaTeX file prepared by the author.